5 November 2025

Deciphering the dynamic nature of the solid-electrolyte interphase in lithium metal batteries

Kun Ryu[1], Yunya Zhang[2], Ethan Jeffs[2], Bin Liu[2], Weikang Li[4], Bhargav Bhamwala[3], Alex Liu[4], Louis Ah[4], Wurigumula Bao[5], Hong Gan[2], Ying Shirley Meng[1,4]

1. University of Chicago
2. SES AI
3. university of california san
4. University of California San Diego
5. University of Chicago

Abstract

Lithium metal batteries (LMBs) promise increased energy densities yet are hindered by rapid capacity fade resulting from the irreversible loss of active lithium (Li). In this study, we investigate the dynamic evolution of the lithium metal anode (LMA) under different charge/discharge conditions through time-resolved characterization of Li morphology, SEI composition, and Li inventory. Fast charging accelerates solvent-driven SEI growth and promotes inactive Li0 accumulation, rapidly depleting active Li and raising safety concerns. In contrast, slow charging facilitates a gradual loss of active Li while promoting the formation of a robust, salt-derived SEI, particularly when combined with fast discharging. The interdependent formation of inactive Li0 and SEI, governed by Butler-Volmer kinetics and electrolyte solvation dynamics, underscores the critical impact of cycling conditions on LMB degradation. These insights provide a mechanistic framework for optimizing cycling protocols to enhance LMB durability and safety.

Keywords

Lithium metal batteries, Solid-electrolyte interphase, Lithium deposition, Surface chemistry, Electrode morphology

https://doi.org/10.26434/chemrxiv-2025-ljjnk

Deciphering the dynamic nature of the solid-electrolyte interphase in lithium metal batteries

Kun Ryu[a#], Yunya Zhang[b#], Ethan Jeffs[b], Bin Liu[b], Weikang Li[c], Bhargav Bhamwala[c], Alex Liu[c], Louis Ah[c], Wurigumula Bao[a*], Hong Gan[b], Ying Shirley Meng[a,c*]*

[a] Pritzker School of Molecular Engineering, University of Chicago, Chicago, IL 60637 USA

[b] SES AI, Woburn, MA 01801, USA

[c] Department of NanoEngineering, University of California San Diego, La Jolla, CA 92093, USA

[#] Authors contributed equally

*Correspondence to: yunyazhang@ses.ai, wubao@uchicago.edu, shirleymeng@uchicago.edu

ABSTRACT

Lithium metal batteries (LMBs) promise increased energy densities yet are hindered by rapid capacity fade resulting from the irreversible loss of active lithium (Li). In this study, we investigate the dynamic evolution of the lithium metal anode (LMA) under different charge/discharge conditions through time-resolved characterization of Li morphology, SEI composition, and Li inventory. Fast charging accelerates solvent-driven SEI growth and promotes inactive Li^0 accumulation, rapidly depleting active Li and raising safety concerns. In contrast, slow charging facilitates a gradual loss of active Li while promoting the formation of a robust, salt-derived SEI, particularly when combined with fast discharging. The interdependent formation of inactive Li^0 and SEI, governed by Butler-Volmer kinetics and electrolyte solvation dynamics, underscores the

critical impact of cycling conditions on LMB degradation. These insights provide a mechanistic framework for optimizing cycling protocols to enhance LMB durability and safety.

INTRODUCTION

Li metal is widely regarded as a key component to achieving energy densities surpassing those of current Li-ion battery technology[1,2]. Nevertheless, the practical application of LMBs is constrained by limited cycling stability, primarily due to the limited plating/stripping coulombic efficiency (CE)[3]. While degradation mechanisms in LMBs are not fully elucidated, empirical evidence identifies the irreversible loss of the active Li inventory, composed of the inactive metallic Li^0 and solid-electrolyte interphase (SEI), as the primary driver of performance decay[4]. Prior investigations have identified the root cause of the formation of inactive metallic Li^0 attributed to the morphology of Li deposits[5,6]. Li deposits with whisker-like morphology and large tortuosity are particularly susceptible to losing electrical connectivity, leaving behind inactive Li^0. Moreover, inactive Li^0 not only consumes the active Li inventory, but also introduces safety risks due to its inherent reactivity. To address these issues, research efforts have focused on strategies to promote compact and uniform Li deposition. Approaches such as applying mechanical pressure, tailoring the electrolyte solvation structure, and incorporating functionalized substrates or protection layers have demonstrated potential in suppressing dendritic growth, thereby inhibiting inactive Li^0 formation[7-15].

Meanwhile, the SEI remains poorly understood due to its complex formation via electrolyte decomposition driven by the thermodynamic mismatch between the high Fermi level of Li and low lowest unoccupied molecular orbital (LUMO) of the electrolyte[16,17]. Ideally, the SEI should be a self-passivating layer that is ionically conductive, electronically insulating, mechanically

robust, and chemically stable against the Li and electrolyte[18-20]. However, inherent chemical and mechanical instabilities cause fractures during Li plating/stripping, triggering SEI reconstruction[21,22]. These fractures create localized ionic conductivity gradients that promote uneven Li deposition and subsequent formation of inactive Li^0. This repetitive process depletes the Li inventory and electrolyte and accumulates SEI residues, leading to reduced CE and accelerated impedance increase, ultimately leading to premature cell failure.

Numerous studies have directly visualized or characterized the dual-layer SEI with an inorganic-rich inner layer and organic-rich outer layer using cryo-electron microscopy (cryo-EM), X-ray photoelectron spectroscopy (XPS), time-of-flight secondary ion mass spectrometry (ToF-SIMS), and electron energy loss spectroscopy[23-27]. Hobold, et al. identified correlation between CE and prevalence of Li_2O within the SEI[28]. Zhang, et al. used cryo-EM to reveal that the SEI undergoes substantial swelling with the electrolyte and correlated higher CE with less mechanical expansion of the SEI[23]. While these findings reveal the chemical, physical, and functional properties of the SEI to improve cell performance, the SEI was only investigated under certain conditions, such as the first 10 cycles, slow charging conditions, or under low deposition capacities (< 2 mAh cm^{-2}). To improve the performance, safety, and cycling stability of commercial LMBs, SEI should also be measured under practical conditions (low negative-to-positive capacity ratio, low electrolyte-to-capacity ratio, high (areal) charge capacity, and practical charging conditions).

An often overlooked yet critical factor in understanding degradation mechanisms in LMBs is the dynamic and continuous evolution of the LMA throughout extended cycling. Such perspective has been rarely captured in previous research, which focus only on isolated points such as beginning-of-life (BOL) and end-of-life (EOL). The rate of active Li^0 consumption, inactive Li^0 and SEI-bound Li^+ evolution, solvent and salt decomposition, and capacity fade evolve

dynamically and interdependently, creating a complex feedback network that collectively governs cell performance[29-32]. Continuous tracking reveals intricate shifts in Li deposition morphology, changes in electrolyte decomposition rates, Li inventory redistributions, and all interlinked processes that simultaneously drive changes in the SEI chemistry, composition, and structure. Specifically, analyzing these evolving processes allows for identification of certain knee points where the electrolyte decomposition mechanisms change or there is a sudden drop in active Li inventory. Capturing this dynamic evolution elucidates previously unrecognized mechanisms of degradation, significantly refining predictive modeling capabilities and informing the rational design of targeted mitigation strategies. By addressing the critical gap left by static assessments, such approach not only advances the fundamental understanding of LMB degradation but also guides practical improvements in battery safety, durability, and performance, ultimately accelerating the transition of LMB technologies from research to widespread commercial adoption.

In this work, we investigated the dynamic evolution of active Li^0, inactive Li^0 and SEI-Li^+ upon cycling under three charge/discharge conditions: C/3–D/3, C/5–1D and 1C–D/3 in practical LMBs pouch cells. Detailed quantification analysis on the SEI components were regularly conducted to understand the dynamic nature of the SEI. The SEI chemistry, composition, and spatial heterogeneity was examined through XPS, SEI quantification, and ToF-SIMS, respectively. The characterization techniques revealed that charging and discharging rates jointly dictate SEI chemistry and structure in LMBs. Fast charging accelerates solvent decomposition and dendritic Li growth, producing a porous organic-rich SEI. When paired with slow discharging, the SEI traps electronically isolated Li^0 and exacerbates SEI growth, capacity fade, and safety risks. In contrast, slow charging favors inorganic, salt-derived species and yields a uniform, layered SEI, while fast discharge produces a dense, inorganic-rich interphase with a lower stripping barrier that curbs

inactive Li^0 accumulation. Quantitative monitoring over hundreds of cycles reveals that even under slow-charge/fast-discharge conditions that initially facilitate anion-decomposition, extended cycling leads to a progressive shift towards solvent-derived products after approximately 200 cycles. This dynamic, rate- and cycle-dependent evolution underscores the need for continuous SEI analysis throughout cycling to fully understand LMA degradation. These insights into SEI dynamics and LMA degradation mechanisms provide essential knowledge for optimizing cycling conditions, particularly in practical applications such as electric vehicles (EVs), where the balance between rapid charging capabilities and stable, prolonged discharge is critical to achieving both long-term battery performance and safety.

RESULTS and DISCUSSION

Mapping the Li inventory

LMB pouch cells with capacity of 270 mAh were fabricated by SES AI using non-aqueous, high-concentration electrolytes (**Figure S1**). Cells were cycled under three distinct charge-discharge rates: 1C charge-D/3 discharge, C/3 charge-D/3 discharge, and C/5 charge-1D discharge. Cycling was terminated upon reaching 80 % capacity retention and was defined as EOL. To investigate the LMA evolution upon cycles, multiple pouch cells were disassembled at 0% state of charge (SOC) after predefined cycle counts, with a minimum of five cells analyzed per condition to establish degradation trends (**Figure 1**). In cycled LMA, Li inventory comprising active Li^0, inactive Li^0, and SEI-incorporated Li^+, was quantified via titration gas chromatography (TGC) and inductively coupled plasma mass spectrometry (ICP-MS) methodology as described in our previous work (**Figures S2** and **S3**)[4,33,34]. Notably, the separators were extracted together with the LMAs for quantification, as optical imaging revealed black dots on their surfaces. SEM analysis and TGC

results further confirmed the presence of dead Li attached to the separators. (**Figure S4**). These observations suggest that inactive Li^0 strongly adheres to the separator. A cross-sectional analysis further confirmed that Li was confined to the separator surface, with no evidence of Li penetration (**Figure S5**). EDX analysis detected a pronounced carbon signal across the separator, accompanied by fluorine and sulfur signals, attributed to the SEI or entrapped salt within the separator matrix (**Figure S6**). Metallic Li^0 quantification using TGC further verified the presence of entrapped Li0 within the SEI (**Figures S7 and S8**). Given these findings, the separators were incorporated into the overall Li inventory quantification.

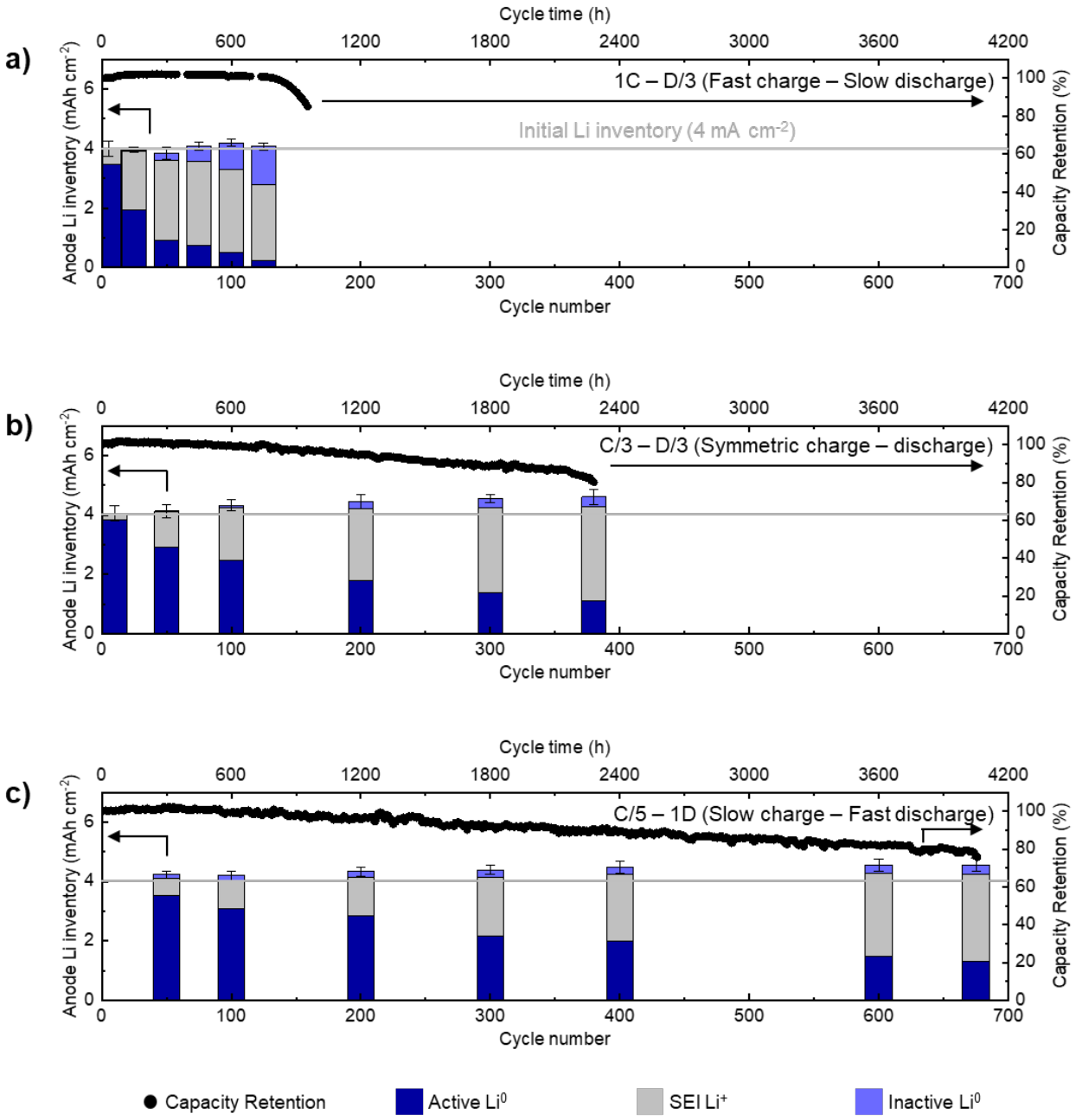

Figure 1. Capacity mapping of active, inactive, and SEI Li under **(a)** 1C–D/3, **(b)** C/3–D/3, and **(c)** C/5–1D of 270 mAh pouch cells employing 4 mAh cm^{-2} cathode and 4 mAh cm^{-2} Li metal anode. The initial Li inventory has been marked by the gray line. Total cycling time is noted on the top x-axis.

Figure 1 shows the cycling performance and the evolution of active Li^0, inactive Li^0, and SEI Li^+ under 1C–D/3, C/3–D/3, and C/5–1D cycling conditions. Consistent with our previous research, cells cycled under C/5–1D exhibited superior cycling stability, achieving EOL after 670

cycles[34]. In contrast, the cell cycled at 1C–D/3 resulted in accelerated degradation, with EOL attained within 160 cycles. Post-mortem analysis of the NMC cathodes, investigated in our previous paper, revealed minimal structural or performance degradation after 50 cycles, suggesting that capacity fade under 1C–D/3 cycling condition primarily originates from LMA deterioration[34]. Under the fast charge and slow discharge (1C–D/3) protocol, the LMA exhibited a rapid depletion of active Li^0, with approximately 74% capacity loss within the first 50 cycles and near-total depletion by EOL (**Figure 1a**). This accelerated initial degradation correlated closely with rapid SEI formation, as SEI-bound Li^+ comprised 75% of the total Li inventory within 75 cycles, maintaining this proportion until EOL. Concurrently, inactive Li^0 continuously accumulated, eventually accounting for approximately 35% of the total Li inventory at EOL. These findings indicate that early-stage capacity loss predominantly arises from extensive SEI formation, while prolonged cycling exacerbates performance deterioration due to the progressive accumulation of inactive Li^0. In contrast, under the symmetric slow charge and discharge (C/3–D/3) protocol, the depletion of active Li^0 and growth of SEI-bound Li^+ occurred more gradually (**Figure 1b**). At EOL, active Li^0 constituted 32.6% of the total Li inventory, implying that Li inventory depletion was not the primary cause of cell failure. Inactive Li^0 formation was also significantly reduced, stabilizing at approximately 8.7% of the total Li inventory. These observations indicate that slower charging protocols facilitate a gradual transformation of active Li^0 into SEI-bound Li^+, contrasting notably with the rapid depletion observed in the fast charge–slow discharge (1C–D/3) protocol. Under the slow charge with fast discharge (C/5–1D) protocol, notable improvements in electrochemical performance were achieved, with 36.2% of Li inventory remaining as active Li^0 at EOL (**Figure 1c**). Additionally, the accumulation of SEI-bound Li^+ and inactive Li^0 progressed more slowly, with inactive Li^0 reaching only 7.5% of the total Li inventory. By EOL under the C/5–1D cycling

protocol, the total cell cycling duration exceeded 4000 hours (approximately 170 days), which is sufficiently extensive to induce notable corrosion within the LMA[23]. This extended exposure suggests that corrosion-related side reactions, potentially involving electrolyte decomposition and interaction with cell components, may significantly contribute to long-term performance degradation. Another reason for the degradation may come from the cathode, which may have cracking and surface phase transformation after long cycles, leading to gradual capacity decay (**Figure S9**).

These experimental findings provide three critical insights into LMB degradation mechanisms under varying cycling protocols. First, rapid charging (1C–D/3) promotes early, aggressive SEI formation that swiftly diminishes active Li^0 inventory, rapidly increases interfacial impedance, and generates uneven Li flux, concurrently accumulating inactive Li^0. This accelerated degradation not only compromises cycle life but also introduces safety concerns due to substantial inactive Li^0 formation (94.5 mAh). Second, slower charging protocols better preserve active Li^0 inventory and minimize inactive Li^0 formation, suggesting additional Li may originate from electrolyte or cathode sources, given the total Li inventory exceeded the initial inventory of 4 mAh cm^{-2} marked in gray lines[35]. These findings highlight that cycling protocols critically influence both performance and total Li inventory dynamics. Specifically, the decomposition of the electrolyte salts significantly contributes to SEI-Li^+, driving the total Li inventory beyond the initial Li amounts supplied by the anode and cathode[13,36]. Finally, SEI-bound Li^+ consistently represented approximately 75% of the total Li inventory across all protocols at EOL. This underscores that SEI formation significantly contributes to overall cell degradation, necessitating detailed SEI characterization to fully elucidate degradation processes from BOL to EOL in LMBs.

Evolution of the Li metal anode morphology

While Li inventory quantification provides key insights into the overall consumption and capacity fade, visualization of the LMA is crucial for qualitative understanding of the spatial distribution and structural changes of both active Li and SEI-Li. **Figure 2** shows the cross-section morphology of LMAs, after different cycles at 0% SOC. Under 1C–D/3, a pronounced consumption of active Li^0 was observed after 50 cycles, with only 4.5 μm of residual active Li inventory remaining (**Figure 2a**). By EOL (125 cycles), the LMA was predominantly composed of a porous SEI, indicating near-complete active Li^0 consumption (**Figure S10**). Even by 25 cycles, over 50% of the LMA had transitioned to a porous SEI. Our previous work demonstrated that an electronically conductive SEI forms on the Li metal anode when cycling at 1C–D/3, leading to Li deposition on top of the SEI. This exposes fresh Li to the electrolyte every cycle, resulting in continuous loss of active Li inventory. Surface morphology SEM image also exhibited a network structure until 50 cycles, transitioning to charge accumulation effects at EOL, indicative of electronically conductive SEI buildup (**Figure S11**)[34]. Under C/3–D/3, a comparatively thinner SEI layer was observed after 50 cycles (**Figure 2b**). We observe that SEI build-up takes effect between 50 and 100 cycles (**Figure S12**). By 200 cycles, the LMA was similarly dominated by porous SEI-Li, analogous to the 1C–D/3 case. Moreover, the active Li^0 inventory was nearly depleted at EOL cycles, mirroring the cross-sectional morphologies of 1C–D/3. The LMA surfaces exhibited a similar network structure to those observed under 1C–D/3, although the charging-induced accumulation of inactive Li^0 was less pronounced (**Figure S13**). In contrast, minimal Li^0 inventory loss occurred after 50 cycles under C/5–1D, with the SEI retaining a compact structure after 200 cycles (**Figure 2c**). At EOL, active Li^0 consumption was less severe than under 1C–D/3 or C/3–D/3, though overall LMA thickness decreased due to SEI delamination during disassembly. Notably, a distinct boundary between compact Li^0 and porous SEI layers was observed (**Figure**

S14). This distinct interface likely represents a localized stabilization of active Li by a robust, passivating SEI, a phenomenon enabled by reduced polarization under slow charging and fast discharging. In contrast, the porous Li deposition and accelerated Li consumption under 1C–D/3 and C/3–D/3 protocols preclude the formation of such discrete boundaries. Surface morphologies also differed under C/5–1D, displaying smooth and dense SEI, unlike the networks structure observed in other protocols (**Figure S15**).

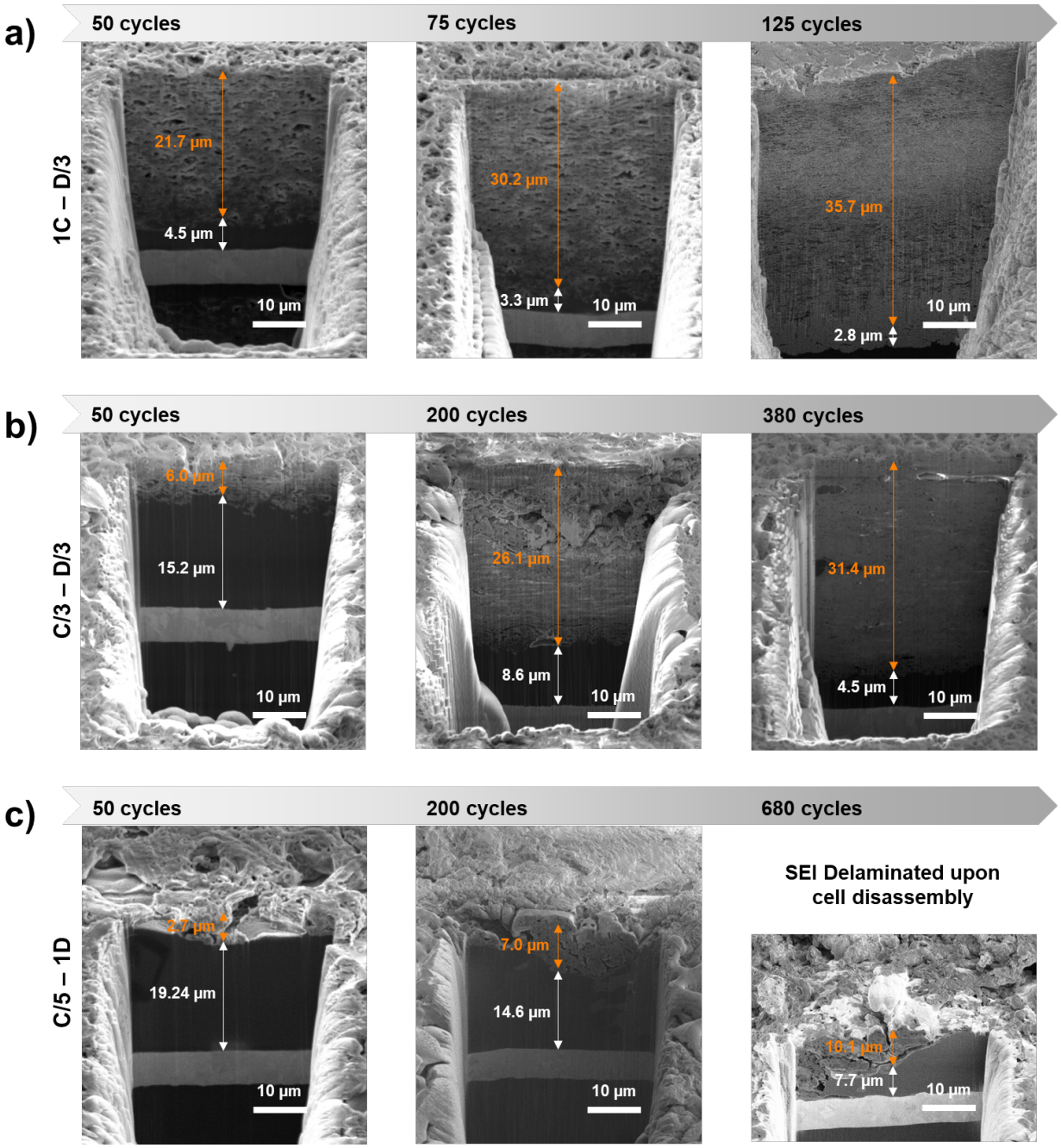

Figure 2. Cross-sectional morphology of Li anode after cycling under **(a)** 1C–D/3, **(b)** C/3–D/3, and **(c)** C/5–1D.

The trends indicate that the plating and stripping behavior of Li metal is inherently unbalanced. This phenomenon can be attributed to the inherent asymmetry between charging and discharging processes in LMAs. According to the Butler–Volmer equation, Li deposition and

stripping follow inherently different kinetics, with a lower activation barrier for deposition than for stripping[37,38]. During charging, the applied electric field enhances the "tip effect", resulting in elevated local areal current densities at protruding regions compared to flat surfaces[6]. During discharging, macroscopic stripping appears uniform, but under slow discharge the curvature-driven dissolution of Li induces filament necking, which electronically isolates metallic Li[39]. This effect is exacerbated during subsequent fast charging, which further accelerates inactive Li^0 buildup[34]. The intrinsic charge–discharge asymmetry in LMBs thereby promotes the incorporation of inactive Li^0 into the SEI. This sequence of events ultimately results in the formation of porous Li networks. Conversely, fast discharging consumes the plated Li, whether dendritic or globular, minimizing the formation of inactive Li^0 within the SEI and permitting Li deposition beneath the SEI.

SEI Chemistry and Quantification

To elucidate the SEI chemistry, XPS was performed on cycled LMAs, with individual peaks integrated and normalized to the total atomic percentage. The XPS of LMAs cycled under all three cycling conditions have an organic-rich outer layer and inorganic-rich inner layer. Under 1C–D/3 cycling conditions, the XPS spectra consistently showed dominant C–C and Li–O(R) peaks, confirming that solvent decomposition is the predominant process (**Figure 3a-c**)[40]. Trace signals corresponding to salt decomposition products (N–S and S–Ox) were detected, and the semi-quantitative analysis revealed negligible contributions from F 1s, N 1s, and S 2p (**Figures S16-19**). In contrast, under C/3–D/3, the emergence of S=O, Li–F, and S–O_x peaks, particularly pronounced at 200 cycles, signal active salt decomposition (**Figures 3d-f** and **S20-22**)[41]. Moreover, the appearance of new C=O further suggests that the electrolyte decomposition pathway evolves under symmetric charge/discharge. XPS profiles at EOL indicate a shift toward dominant solvent

decomposition, as evidenced by increased C–C and Li–O(R) peaks with a rise in C 1s signals (**Figure S20**). These trends actively correlate with the SEI quantification results. Under C/5–1D, the SEI composition remained relatively consistent throughout cycling (**Figures 3g-i** and **S24-27**). A gradual increase in salt decomposition products (S=O, Li–F, S–O_x) was observed, accompanied by a notable decrease in solvent-derived species (C–C and Li–O(R)). The detection of TM–F species in F 1s at EOL indicates that transition metal dissolution from the NMC cathode also contributes to the evolving SEI chemistry[42,43]. Interestingly, while the SEI was initially dominated by major components with fingerprint constituents present only in trace amounts, the proportion of these minor components increased at EOL. This shift results in a more heterogeneous and diverse SEI, likely reflecting the stability of the SEI.

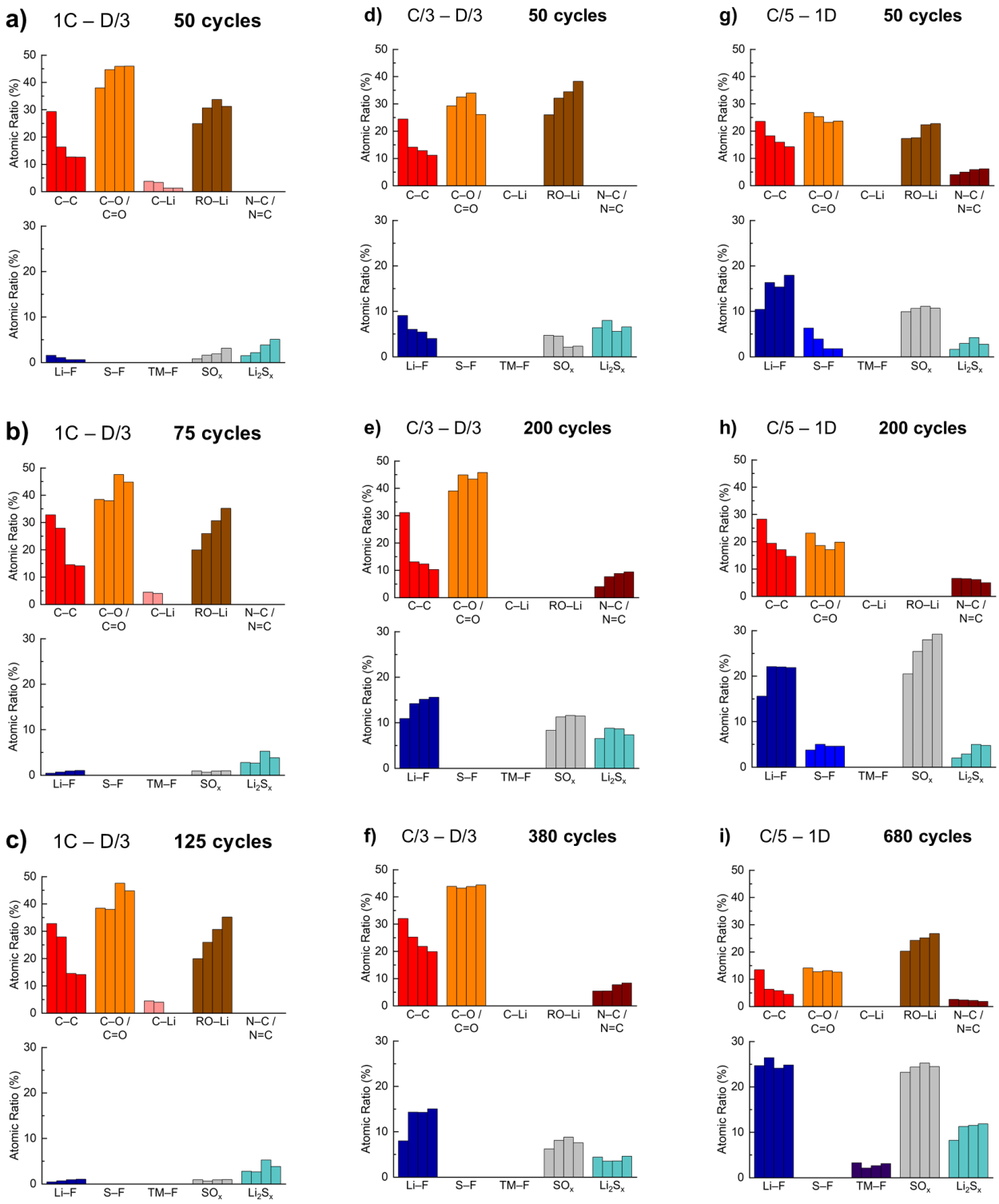

Figure 3. Evolution of atomic species within the LMA under **(a-c)** 1C–D/3, **(d-f)** C/3–D/3, and **(g-i)** C/5–1D analyzed using XPS. Normalized peak intensities obtained by normalizing the integrated peak intensities. Top graph containing C–C, C–O, C=O, C–Li, RO–Li, N–C, and N=C represents the organic species. Bottom graph containing Li^0, Li–F, S–F, TM–F, SO_x, Li_2S_x represents metallic or inorganic SEI species.

Li inventory quantification and cross-sectional morphology indicate that the porous Li comprises the majority of the LMA, particularly near end-of-life. Consequently, a comprehensive quantitative analysis of the SEI was performed to elucidate its evolution. Detailed procedures for quantifying SEI components are illustrated in **Fig. 4a**. Calibration with standard solutions confirmed method accuracy, showing linear correlations ($R^2 > 0.98$) between known concentrations and measured intensities (**Fig. 4b-4f**, **S28,** and **29**). The total Li content measured exceeded the Li loss inferred from capacity fade, indicating that salt decomposition contributes significantly to the SEI formation. The normalized quantities of the inactive Li residuals reveal an increasing proportion of inactive Li^0 under 1C–D/3 (**Fig. 4g**). The overall SEI composition remains relatively stable, suggesting a consistent electrolyte decomposition mechanism throughout cycling (**Fig. S31**). Notably, the SEI contains minimal amounts of sulfur-containing species, LiF, and Li_2O, indicating limited salt decomposition. The majority of the SEI-Li was categorized as unclassified Li species, which is most likely associated with solvent-derived products. This implies active solvent decomposition under fast charging conditions. In contrast, under C/3–D/3 conditions, inactive Li^0 increases more gradually, with predominant formation of Li_2O and LiF species by 100 cycles, suggesting active salt decomposition (**Fig. 4h**)[28,44]. Then, the proportion of inorganic species decreases, suggesting that solvent decomposition becomes predominant after an initially stable, salt-derived SEI is established. Under C/5–1D, the contribution of inactive Li^0 decreases

with cycle number, and the SEI exhibits a higher content of salt decomposition products, with significantly increased levels of LiF and sulfur-containing species compared to C/3–D/3 (**Fig. 4i**). Although salt decomposition is active during the early stages (50–100 cycles), it decelerates by 200 and 400 cycles as solvent decomposition takes over – a trend also observed under C/3–D/3. Interestingly, an increase in salt decomposition is observed at EOL, suggesting that secondary factors may promote the formation of an inorganic-rich SEI during prolonged cycling.

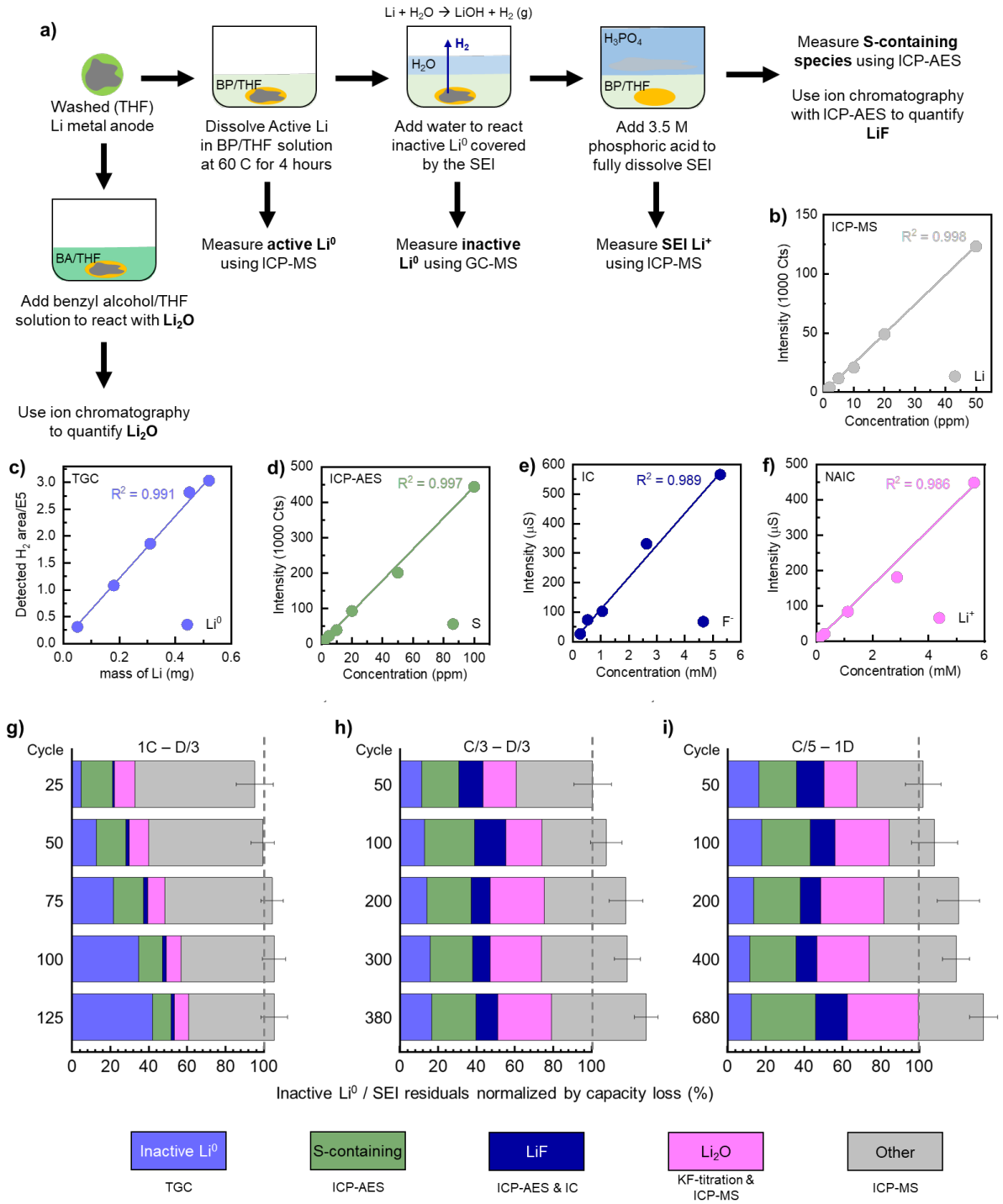

Figure 4. **(a)** Schematic of SEI quantification protocols. Calibration curves of **(b)** ICP-MS used to quantify active Li^0 and SEI Li^+, **(c)** TGC used to quantify inactive Li^0, **(c)** ICP-MS used to quantify active Li^0, SEI Li^+, **(d)** ICP-AES used to quantify S-containing species, **(e)** ion chromatography used to quantify LiF, and **(f)** non-aqueous ion chromatography used to quantify Li_2O. SEI quantification results of cycled LMA under **(g)** 1C–D/3, **(h)** C/3–D/3, and **(i)** C/5–1D.

Spatial mapping of the SEI

To elucidate the spatial heterogeneity of the SEI on Li metal LMAs, ToF-SIMS was employed. After 50 cycles under a 1C–D/3 cycling protocol, the depth profiling revealed a stratified SEI structure (**Fig. 5a**). Specifically, LiF_2^- species were predominantly located in the innermost regions, while LiO^- and LiS^- species were centered at approximately 60 nm from the electrode surface. In contrast, SO_2^- signals were primarily detected near the SEI surface. The presence of SO_2^- at the outermost layers likely indicates the residual salts trapped within the porous network of the SEI. Under slower charging conditions (C/3–D/3 and C/5–1D), the SEI was observed to be thinner, with the principal components exhibiting well-aligned spatial distributions (**Fig. 5b** and **5c**). In particular, LMA cycled under C/3–D/3 initially exhibited a homogenous SEI, which may be more susceptible to degradation over time. In contrast, C/5–1D cycling produced a layered SEI structure, with the innermost layer predominantly enriched in LiF, an intermediate region composed of LiO^- and LiS^- species, and an outer organic layer primarily containing C_2HO^- fragments.

The absolute intensities of the C_2HO^-, LiF_2^-, and LiO^- peaks were compared after 50 cycles (**Fig. S32**). Fast charging yielded increased signals of C_2HO^-, indicating more pronounced solvent decomposition. Conversely, slow charging conditions resulted in significantly higher levels of LiF_2^- and LiO^-, with these inorganic species centered at 40 nm. C/5–1D exhibited a marked increase in LiF_2^- signals compared to C/3–D/3, suggesting increased salt decomposition kinetics under C/5–1D. These results align with the quantitative data from SEI quantification and XPS studies. Extending the cycling to EOL under 1C–D/3, clear trends were not observable, except for the accumulation of SO_2^- at the surface due to the trapped salts. Under C/3–D/3 cycling, SEI exhibited progressive thickening, evidenced by LiF_2^- peak shifting from approximately 30 nm to

50 nm at EOL. Additionally, the deeper penetration of C_2HO^- species under these conditions suggests ongoing solvent decomposition. In contrast, the C/5–1D protocol maintained a well-ordered SEI structure throughout cycling. The spatial localization of these species also provides critical insights into the degradation pathways of lithium bis(fluorosulfonyl)imide (LiFSI) salts. Initially, the cleavage of vulnerable S–F bonds produces LiF, which integrates into the innermost SEI layers. Subsequently, the breakdown of SO_2 groups leads to the formation of Li_2O. With continued cycling and the progressive disruption of S=O bonds, the cleavage of N–S bonds results in the formation of Li_2S and various SO_x species.

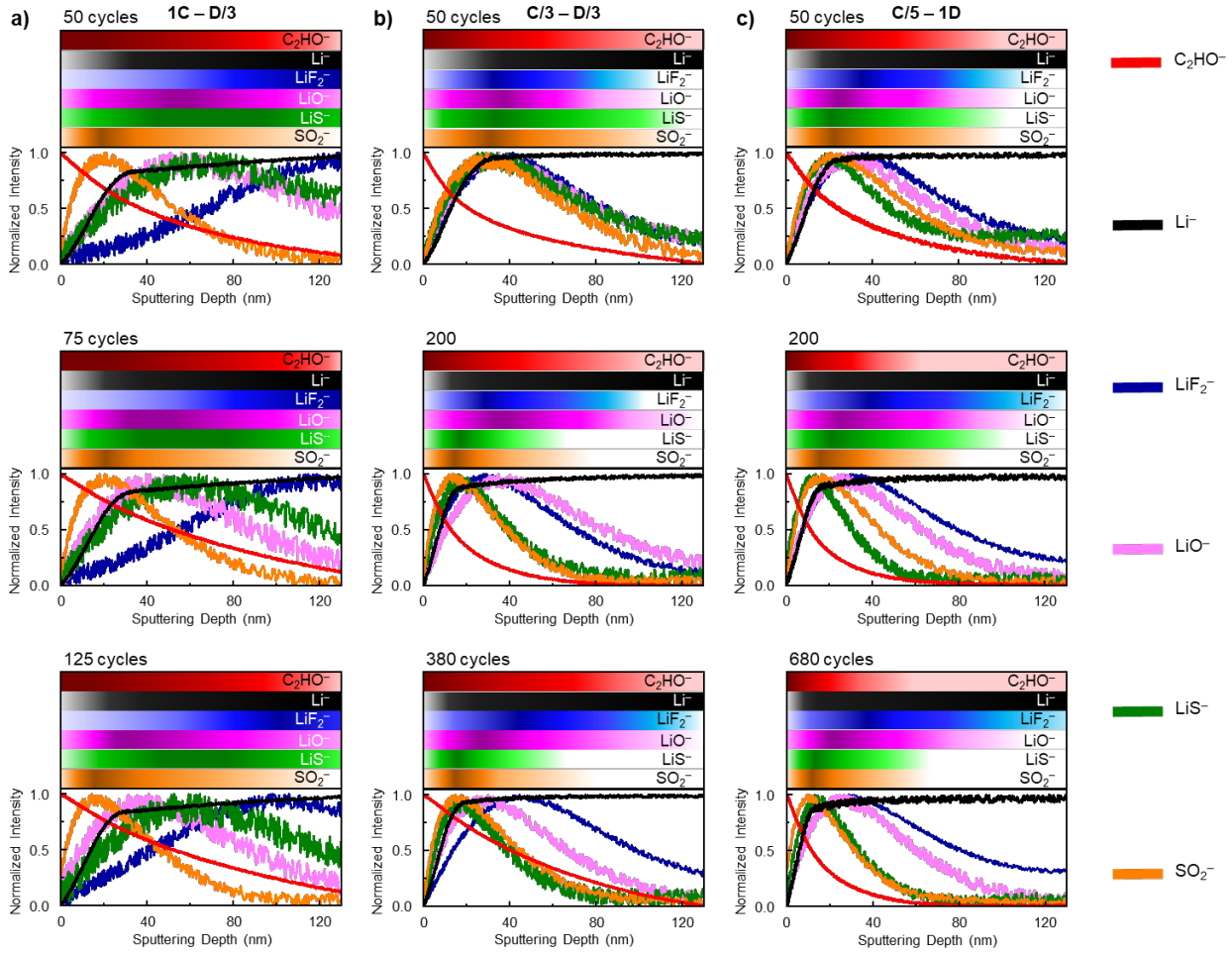

Figure 5. Evolution of SEI structure and its chemical composition under **(a)** 1C–D/3, **(b)** C/3–D/3, and **(c)** C/5–1D.

Effect of charge-discharge rates on Li morphology and SEI chemistry

The LMA characterization results demonstrate the individual contributions of charge and discharge rates to LMB performance. Specifically, slow charging paired with fast discharging optimizes cell performance by preserving active Li^0 inventory and promoting the formation of compact and inorganic-rich SEI. To accurately elucidate these rate-dependent effects, it is imperative to decouple the impacts of charging and discharging rates on the Li morphology and SEI chemistry. The first question is how the charge and discharge rates affect the Li morphology with cycling. Under fast charging (1C–D/3), high Li^+ polarization at the electrode surface promotes non-uniform nucleation and growth of needle-like Li structures (**Fig. 6a**). The local electric field concentrates at protrusion tips, driving vertical dendritic propagation, accelerating parasitic consumption of both Li and solvent. In contrast, implementing a slow charge protocol (C/3–D/3) reduces the Li^+ concentration gradient and polarization at the electrode surface, thereby promoting homogeneous nucleation and lateral Li deposition. Slower charging protocol (C/5–1D) amplifies these effects. This minimizes active Li exposure to electrolyte, suppressing irreversible side reactions and supporting the formation of a denser, more stable SEI. Discharge rates primarily govern Li^0 stripping uniformity. Slow discharge (1C–D/3, C/3–D/3) allows for the system to have time to minimize overpotential and strips Li at low-resistance and high-contact areas like the roots, leaving isolated Li^0 within the SEI. In contrast, the high overpotential forces during fast discharge (C/5–1D) tends to strip Li uniformly. This mitigates the accumulation of inactive Li^0, effectively counterbalancing the intrinsic Butler–Volmer asymmetry that favors plating over stripping. These mechanistic insights align with Li-inventory mapping and FIB-SEM observations. 1C–D/3 exhibits rapid increases in SEI thickness and inactive Li^0 due to dendrite formation and slow stripping. C/3–D/3 shows more uniform plating with slower SEI and inactive Li^0 growth but retains

slight inactive Li^0, whereas C/5–1D achieves minimal loss of active Li^0 to SEI formation or inactive Li^0, confirming that slow charging paired with fast discharging optimally preserves Li^0 inventory and cultivates a stable interphase.

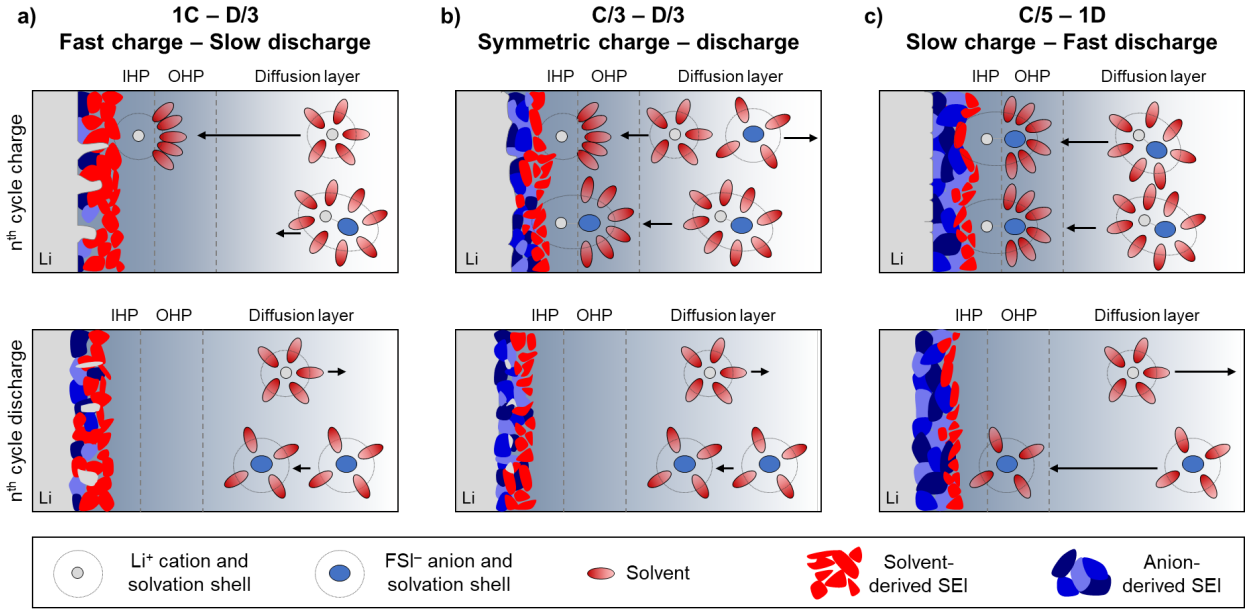

Figure 6. Schematic of Li deposition behavior and SEI formation process under different cycling conditions.

The next critical question is how different cycling conditions influence the chemical properties of the SEI. Bulk electrolytes comprise solvent-separated ion pairs (SSIPs) and contact ion pairs/aggregates (CIP/AGGs), with CIP/AGGs exhibiting larger solvation shells and correspondingly lower diffusivity (as described by the Stokes–Einstein equation)[45-48]. Under fast (1C–D/3) charging, high polarization drives SSIPs—with smaller solvation radii and higher mobility—toward the LMA surface. Their solvent-rich solvation shells decompose preferentially, forming organic-dominated SEI layers. In contrast, slow (C/3–D/3, C/5–1D) charging permits CIP/AGGs, which have anion-rich coordination, to migrate to the interface, thereby enabling anion decomposition and promoting the growth of an inorganic-rich SEI. Moreover, fast discharging

further enriches the LMA's double layer with SSIP–anion species, which decompose during subsequent charging to reinforce inorganic content (**Fig. 6c**). Together, slow charging followed by fast discharging maximizes the incorporation of anion-derived components in the SEI. Integrating the influence of charge-discharge rates on Li morphology reveals that fast charging paired with slow discharging promotes solvent-driven SEI formation over dendritic Li, yielding mechanically weak, organic interphases[40, 49-52]. These unstable SEIs fracture during cycling, perpetually exposing fresh Li^0 and accelerating both Li and electrolyte consumption due to their whisker-like morphology. In contrast, slow charging-fast discharging promotes the development of an anion-derived robust SEI atop uniformly deposited Li, thereby minimizing the active Li^0 loss and enhancing cycling stability.

CONCLUSION

In summary, we reveal the dynamic evolution of the LMA, characterized by progressive changes in the Li inventory, LMA morphology, and SEI chemistry and structure. Our results show that fast charging accelerates solvent decomposition and promotes dendritic Li growth, resulting in a porous, organic-rich SEI that is structurally fragile and prone to breakage. When combined with slow discharging, the limited stripping driving force—along with the resistive nature of the porous SEI—impedes uniform Li removal, causing metallic Li^0 to become electronically isolated and accumulate as inactive Li. Over extended cycling, this configuration exacerbates interfacial degradation, leading to excessive SEI formation, accelerated capacity fade, and elevated safety risks.

Slow charging combined with fast discharging promotes the formation of a robust, inorganic-rich SEI and better preserves active Li^0 by reducing the stripping barrier and limiting

inactive Li^0 accumulation. This effect is evident under C/5–1D conditions and is consistent with our prior finding that higher discharge rates shift Li deposition beneath the SEI (1C-6C), underscoring the critical role of discharge kinetics in interfacial stability[34]. Further analysis shows that under C/5–1D and C/3–D/3, the SEI is initially enriched with salt decomposition products, but this trend slows as cycling progresses and solvent decomposition becomes dominant. A resurgence of salt-derived species at end-of-life suggests that the SEI continues to evolve dynamically, driven by ongoing electrolyte consumption, which is crucial for sustaining long-term cycling performance. Quantitative tracking of SEI-bound Li^+ and inactive Li^0 provides valuable mechanistic insight into how discharge conditions influence interfacial stability and degradation pathways. These findings emphasize that optimizing Li stripping kinetics is key to enhancing Li utilization efficiency and maintaining SEI integrity over prolonged cycling.

ASSOCIATED CONTENT

Data Availability Statement

The data that support the findings of this study are available from the corresponding author upon reasonable request.

AUTHOR INFORMATION

Corresponding Author

*(Y.Z.)Yunya Zhang E-mail: yunyazhang@ses.ai

*(W.B.)Wurigumula Bao E-mail: wubao@uchicago.edu
ORCID:
Wurigumula Bao: 0000-0001-8109-1546

*(Y.SM.) E-mail: shirleymeng@uchicago.edu;
ORCID:
Ying Shirley Meng: 0000-0001-8936-8845

*(H.G.) E-mail: hong@ses.ai;

Conflict of Interest

The authors declare no conflicts of interest. The authors declare the following competing financial interest(s): Ying Shirley Meng is a technical advisor for SES AI.

AUTHOR CONTRIBUTIONS

Y.Z., W.B., H.G., and Y.S.M. conceived the ideas. K.R. wrote the manuscript. E.J. and Y.Z. prepared electrodes and cycled the cells. W.B., K.R., B.B., and L.A. performed TGC measurements. W.B., K.R. and A. L. performed Cryo-FIB/SEM. W.B., W.L. and K.R. designed and conducted XPS experiments. K.R. performed the Tof-SIMS experiment. All authors discussed the results and commented on the manuscript, and haven given approval to the final version of the manuscript.

FUNDING SOURCES

This work was supported by the SES AI. XPS and ToF-SIMS used the Keck-II facility (RRID: SCR_026360) of Northwestern University's NUANCE Center, which has received support from the SHyNE Resource (NSF ECCS-2025633), the IIN, and Northwestern's MRSEC program (NSF DMR-2308691). FIB-SEM was performed using the ThermoFisher Helios 5CX (cryo)FIB-SEM instrument in the Electron Microscopy Core of UIC's Research Resources Center (support from UIC, Northwestern University and ARO (W911NF2110052).) and FEI Scios DualBeam FIB/SEM at San Diego Nanotechnology Infrastructure (SDNI) (supported by the National Science Foundation (Grant ECCS-1542148)). ICP-MS, ICP-OES, and IC were performed at the Northwestern University Quantitative Bio-element Imaging Center, generously supported by NASA Ames Research Center NNA06CB93G. The authors acknowledge the use of facilities and instrumentation at the UC Irvine Materials Research Institute (IMRI), which is supported in part by the National Science Foundation through the UC Irvine Materials Research Science and Engineering Center (DMR-2011967). Specifically, the XPS work was performed using instrumentation funded in part by the National Science Foundation Major Research Instrumentation Program under grant no. CHE-1338173.

References

1. Zhang, X.; Yang, Y.; Zhou, Z. Towards Practical Lithium-Metal Anodes. *Chem. Soc. Rev.* **2020**, *49* (10), 3040–3071. https://doi.org/10.1039/C9CS00838A.
2. Lin, D.; Liu, Y.; Cui, Y. Reviving the Lithium Metal Anode for High-Energy Batteries. *Nature Nanotech* **2017**, *12* (3), 194–206. https://doi.org/10.1038/nnano.2017.16.
3. Hobold, G. M.; Lopez, J.; Guo, R.; Minafra, N.; Banerjee, A.; Shirley Meng, Y.; Shao-Horn, Y.; Gallant, B. M. Moving beyond 99.9% Coulombic Efficiency for Lithium Anodes in Liquid Electrolytes. *Nat Energy* **2021**, *6* (10), 951–960. https://doi.org/10.1038/s41560-021-00910-w.
4. Deng, W.; Yin, X.; Bao, W.; Zhou, X.; Hu, Z.; He, B.; Qiu, B.; Meng, Y. S.; Liu, Z. Quantification of Reversible and Irreversible Lithium in Practical Lithium-Metal Batteries. *Nat Energy* **2022**, *7* (11), 1031–1041. https://doi.org/10.1038/s41560-022-01120-8.
5. Wu, Z.; Wang, C.; Hui, Z.; Liu, H.; Wang, S.; Yu, S.; Xing, X.; Holoubek, J.; Miao, Q.; Xin, H. L.; Liu, P. Growing Single-Crystalline Seeds on Lithiophobic Substrates to Enable Fast-Charging Lithium-Metal Batteries. *Nat Energy* **2023**. https://doi.org/10.1038/s41560-023-01202-1.
6. Yuan, X.; Liu, B.; Mecklenburg, M.; Li, Y. Ultrafast Deposition of Faceted Lithium Polyhedra by Outpacing SEI Formation. *Nature* **2023**, *620* (7972), 86–91. https://doi.org/10.1038/s41586-023-06235-w.
7. Liu, Y.; Tao, X.; Wang, Y.; Jiang, C.; Ma, C.; Sheng, O.; Lu, G.; Lou, X. W. (David). Self-Assembled Monolayers Direct a LiF-Rich Interphase toward Long-Life Lithium Metal Batteries. *Science* **2022**, *375* (6582), 739–745. https://doi.org/10.1126/science.abn1818.
8. Kim, M. S.; Zhang, Z.; Rudnicki, P. E.; Yu, Z.; Wang, J.; Wang, H.; Oyakhire, S. T.; Chen, Y.; Kim, S. C.; Zhang, W.; Boyle, D. T.; Kong, X.; Xu, R.; Huang, Z.; Huang, W.; Bent, S. F.; Wang, L.-W.; Qin, J.; Bao, Z.; Cui, Y. Suspension Electrolyte with Modified Li+ Solvation Environment for Lithium Metal Batteries. *Nat. Mater.* **2022**, *21* (4), 445–454. https://doi.org/10.1038/s41563-021-01172-3.
9. (Ryu, K.; Lee, K.; Lim, J.; Lee, M. J.; Kim, K.-H.; Lee, U. H.; Rinkel, B. L. D.; Kim, K.; Kim, S.; Kim, D.; Shin, D.; McCloskey, B.; Kang, J.; Lee, S. W. Additive Engineering Strategies for Improved Interfacial Stability in Lithium Metal Batteries. *Energy Environ. Sci.* **2024**, *17* (20), 7772–7781. https://doi.org/10.1039/D4EE02479F.
10. Baran, M. J.; Carrington, M. E.; Sahu, S.; Baskin, A.; Song, J.; Baird, M. A.; Han, K. S.; Mueller, K. T.; Teat, S. J.; Meckler, S. M.; Fu, C.; Prendergast, D.; Helms, B. A. Diversity-

Oriented Synthesis of Polymer Membranes with Ion Solvation Cages. *Nature* **2021**, *592* (7853), 225–231. https://doi.org/10.1038/s41586-021-03377-7.

11. Ren, X.; Zou, L.; Cao, X.; Engelhard, M. H.; Liu, W.; Burton, S. D.; Lee, H.; Niu, C.; Matthews, B. E.; Zhu, Z.; Wang, C.; Arey, B. W.; Xiao, J.; Liu, J.; Zhang, J.-G.; Xu, W. Enabling High-Voltage Lithium-Metal Batteries under Practical Conditions. *Joule* **2019**, *3* (7), 1662–1676. https://doi.org/10.1016/j.joule.2019.05.006.
12. Kim, S.-H.; Kim, M.; Kristanto, I.; Kim, W.-Y.; Ryu, K.; Kim, H.-I.; Ma, K. Y.; Heo, C.; Kim, H.; Kwak, S. K.; Meng, Y. S.; Shin, H. S.; Lee, S.-Y. Horizontal Lithium Electrodeposition on Atomically Polarized Monolayer Hexagonal Boron Nitride. *ACS Nano* **2024**, *18* (35), 24128–24138. https://doi.org/10.1021/acsnano.4c05208.
13. Ren, X.; Chen, S.; Lee, H.; Mei, D.; Engelhard, M. H.; Burton, S. D.; Zhao, W.; Zheng, J.; Li, Q.; Ding, M. S.; Schroeder, M.; Alvarado, J.; Xu, K.; Meng, Y. S.; Liu, J.; Zhang, J.-G.; Xu, W. Localized High-Concentration Sulfone Electrolytes for High-Efficiency Lithium-Metal Batteries. *Chem* **2018**, *4* (8), 1877–1892. https://doi.org/10.1016/j.chempr.2018.05.002.
14. Yu, Z.; Wang, H.; Kong, X.; Huang, W.; Tsao, Y.; Mackanic, D. G.; Wang, K.; Wang, X.; Huang, W.; Choudhury, S.; Zheng, Y.; Amanchukwu, C. V.; Hung, S. T.; Ma, Y.; Lomeli, E. G.; Qin, J.; Cui, Y.; Bao, Z. Molecular Design for Electrolyte Solvents Enabling Energy-Dense and Long-Cycling Lithium Metal Batteries. *Nat Energy* **2020**, *5* (7), 526–533. https://doi.org/10.1038/s41560-020-0634-5.
15. Fang, C.; Lu, B.; Pawar, G.; Zhang, M.; Cheng, D.; Chen, S.; Ceja, M.; Doux, J.-M.; Musrock, H.; Cai, M.; Liaw, B.; Meng, Y. S. Pressure-Tailored Lithium Deposition and Dissolution in Lithium Metal Batteries. *Nat Energy* **2021**, *6* (10), 987–994. https://doi.org/10.1038/s41560-021-00917-3.
16. Goodenough, J. B.; Park, K.-S. The Li-Ion Rechargeable Battery: A Perspective. *J. Am. Chem. Soc.* **2013**, *135* (4), 1167–1176. https://doi.org/10.1021/ja3091438.
17. Gauthier, M.; Carney, T. J.; Grimaud, A.; Giordano, L.; Pour, N.; Chang, H.-H.; Fenning, D. P.; Lux, S. F.; Paschos, O.; Bauer, C.; Maglia, F.; Lupart, S.; Lamp, P.; Shao-Horn, Y. Electrode–Electrolyte Interface in Li-Ion Batteries: Current Understanding and New Insights. *J. Phys. Chem. Lett.* **2015**, *6* (22), 4653–4672. https://doi.org/10.1021/acs.jpclett.5b01727.
18. Ko, S.; Obukata, T.; Shimada, T.; Takenaka, N.; Nakayama, M.; Yamada, A.; Yamada, Y. Electrode Potential Influences the Reversibility of Lithium-Metal Anodes. *Nat Energy* **2022**, *7* (12), 1217–1224. https://doi.org/10.1038/s41560-022-01144-0.

19. Liu, J.; Bao, Z.; Cui, Y.; Dufek, E. J.; Goodenough, J. B.; Khalifah, P.; Li, Q.; Liaw, B. Y.; Liu, P.; Manthiram, A.; Meng, Y. S.; Subramanian, V. R.; Toney, M. F.; Viswanathan, V. V.; Whittingham, M. S.; Xiao, J.; Xu, W.; Yang, J.; Yang, X.-Q.; Zhang, J.-G. Pathways for Practical High-Energy Long-Cycling Lithium Metal Batteries. *Nat Energy* **2019**, *4* (3), 180–186. https://doi.org/10.1038/s41560-019-0338-x.
20. Zhang, S.; Li, R.; Hu, N.; Deng, T.; Weng, S.; Wu, Z.; Lu, D.; Zhang, H.; Zhang, J.; Wang, X.; Chen, L.; Fan, L.; Fan, X. Tackling Realistic Li+ Flux for High-Energy Lithium Metal Batteries. *Nat Commun* **2022**, *13* (1), 5431. https://doi.org/10.1038/s41467-022-33151-w.
21. Gao, Y.; Du, X.; Hou, Z.; Shen, X.; Mai, Y.-W.; Tarascon, J.-M.; Zhang, B. Unraveling the Mechanical Origin of Stable Solid Electrolyte Interphase. *Joule* **2021**, *5* (7), 1860–1872. https://doi.org/10.1016/j.joule.2021.05.015.
22. Heiskanen, S. K.; Kim, J.; Lucht, B. L. Generation and Evolution of the Solid Electrolyte Interphase of Lithium-Ion Batteries. *Joule* **2019**, *3* (10), 2322–2333. https://doi.org/10.1016/j.joule.2019.08.018.
23. Zhang, Z.; Li, Y.; Xu, R.; Zhou, W.; Li, Y.; Oyakhire, S. T.; Wu, Y.; Xu, J.; Wang, H.; Yu, Z.; Boyle, D. T.; Huang, W.; Ye, Y.; Chen, H.; Wan, J.; Bao, Z.; Chiu, W.; Cui, Y. Capturing the Swelling of Solid-Electrolyte Interphase in Lithium Metal Batteries. *Science* **2022**, *375* (6576), 66–70. https://doi.org/10.1126/science.abi8703.
24. Wi, T.-U.; Park, S. O.; Yeom, S. J.; Kim, M.-H.; Kristanto, I.; Wang, H.; Kwak, S. K.; Lee, H.-W. Revealing the Dual-Layered Solid Electrolyte Interphase on Lithium Metal Anodes via Cryogenic Electron Microscopy. *ACS Energy Lett.* **2023**, *8* (5), 2193–2200. https://doi.org/10.1021/acsenergylett.3c00505.
25. Li, T.; Zhang, X.-Q.; Shi, P.; Zhang, Q. Fluorinated Solid-Electrolyte Interphase in High-Voltage Lithium Metal Batteries. *Joule* **2019**, *3* (11), 2647–2661. https://doi.org/10.1016/j.joule.2019.09.022.
26. Yang, Y.; Davies, D. M.; Yin, Y.; Borodin, O.; Lee, J. Z.; Fang, C.; Olguin, M.; Zhang, Y.; Sablina, E. S.; Wang, X.; Rustomji, C. S.; Meng, Y. S. High-Efficiency Lithium-Metal Anode Enabled by Liquefied Gas Electrolytes. *Joule* **2019**, *3* (8), 1986–2000. https://doi.org/10.1016/j.joule.2019.06.008.
27. Wang, J.; Huang, W.; Pei, A.; Li, Y.; Shi, F.; Yu, X.; Cui, Y. Improving Cyclability of Li Metal Batteries at Elevated Temperatures and Its Origin Revealed by Cryo-Electron Microscopy. *Nat Energy* **2019**, *4* (8), 664–670. https://doi.org/10.1038/s41560-019-0413-3.
28. Hobold, G. M.; Wang, C.; Steinberg, K.; Li, Y.; Gallant, B. M. High Lithium Oxide Prevalence in the Lithium Solid–Electrolyte Interphase for High Coulombic Efficiency. *Nat Energy* **2024**, *9* (5), 580–591. https://doi.org/10.1038/s41560-024-01494-x.

29. Bi, C.; Zhu, Y.; Li, Z.; Zhao, M.; Zhang, X.; Li, B.; Huang, J. Evolution of Lithium Metal Anode Along Cycling in Working Lithium–Sulfur Batteries. *Advanced Energy Materials* **2024**, *14* (39), 2402609. https://doi.org/10.1002/aenm.202402609.
30. Ding, J.; Xu, R.; Ma, X.; Xiao, Y.; Yao, Y.; Yan, C.; Huang, J. Quantification of the Dynamic Interface Evolution in High-Efficiency Working Li-Metal Batteries. *Angewandte Chemie* **2022**, *134* (13), e202115602. https://doi.org/10.1002/ange.202115602.
31. Weber, R.; Genovese, M.; Louli, A. J.; Hames, S.; Martin, C.; Hill, I. G.; Dahn, J. R. Long Cycle Life and Dendrite-Free Lithium Morphology in Anode-Free Lithium Pouch Cells Enabled by a Dual-Salt Liquid Electrolyte. *Nat Energy* **2019**, *4* (8), 683–689. https://doi.org/10.1038/s41560-019-0428-9.
32. Tan, S.; Kim, J.-M.; Corrao, A.; Ghose, S.; Zhong, H.; Rui, N.; Wang, X.; Senanayake, S.; Polzin, B. J.; Khalifah, P.; Xiao, J.; Liu, J.; Xu, K.; Yang, X.-Q.; Cao, X.; Hu, E. Unravelling the Convoluted and Dynamic Interphasial Mechanisms on Li Metal Anodes. *Nat. Nanotechnol.* **2023**, *18* (3), 243–249. https://doi.org/10.1038/s41565-022-01273-3.
33. Fang, C.; Li, J.; Zhang, M.; Zhang, Y.; Yang, F.; Lee, J. Z.; Lee, M.-H.; Alvarado, J.; Schroeder, M. A.; Yang, Y.; Lu, B.; Williams, N.; Ceja, M.; Yang, L.; Cai, M.; Gu, J.; Xu, K.; Wang, X.; Meng, Y. S. Quantifying Inactive Lithium in Lithium Metal Batteries. *Nature* **2019**, *572* (7770), 511–515. https://doi.org/10.1038/s41586-019-1481-z.
34. Zhang, Y.; Bao, W.; Jeffs, E.; Liu, B.; Han, B.; Mai, W.; Li, X.; Li, W.; Xu, Y.; Bhamwala, B.; Liu, A.; Ah, L.; Ryu, K.; Meng, Y. S.; Gan, H. Unveiling the Impacts of Charge/Discharge Rate on the Cycling Performance of Li-Metal Batteries. *ACS Energy Lett.* **2025**, 872–880. https://doi.org/10.1021/acsenergylett.4c03215.
35. Gervillié-Mouravieff, C.; Ah, L.; Liu, A.; Huang, C.-J.; Meng, Y. S. Deciphering the Impact of the Active Lithium Reservoir in Anode-Free Pouch Cells. *ACS Energy Lett.* **2024**, *9* (4), 1693–1700. https://doi.org/10.1021/acsenergylett.4c00457.
36. Cao, X.; Ren, X.; Zou, L.; Engelhard, M. H.; Huang, W.; Wang, H.; Matthews, B. E.; Lee, H.; Niu, C.; Arey, B. W.; Cui, Y.; Wang, C.; Xiao, J.; Liu, J.; Xu, W.; Zhang, J.-G. Monolithic Solid–Electrolyte Interphases Formed in Fluorinated Orthoformate-Based Electrolytes Minimize Li Depletion and Pulverization. *Nat Energy* **2019**, *4* (9), 796–805. https://doi.org/10.1038/s41560-019-0464-5.
37. Jiang, F.; Yang, S.; Liu, H.; Cheng, X.; Liu, L.; Xiang, R.; Zhang, Q.; Kaskel, S.; Huang, J. Mechanism Understanding for Stripping Electrochemistry of Li Metal Anode. *SusMat* **2021**, *1* (4), 506–536. https://doi.org/10.1002/sus2.37.

38. Gao, X.; Zhou, Y.-N.; Han, D.; Zhou, J.; Zhou, D.; Tang, W.; Goodenough, J. B. Thermodynamic Understanding of Li-Dendrite Formation. *Joule* **2020**, *4* (9), 1864–1879. https://doi.org/10.1016/j.joule.2020.06.016.
39. Zhang, J.; Chadwick, A. F.; Voorhees, P. W. Isolated Metallic Lithium Formation in Lithium-Metal Batteries. *Cell Reports Physical Science* **2025**, *6* (1), 102360. https://doi.org/10.1016/j.xcrp.2024.102360.
40. Cao, X.; Ren, X.; Zou, L.; Engelhard, M. H.; Huang, W.; Wang, H.; Matthews, B. E.; Lee, H.; Niu, C.; Arey, B. W.; Cui, Y.; Wang, C.; Xiao, J.; Liu, J.; Xu, W.; Zhang, J.-G. Monolithic Solid–Electrolyte Interphases Formed in Fluorinated Orthoformate-Based Electrolytes Minimize Li Depletion and Pulverization. *Nat Energy* **2019**, *4* (9), 796–805. https://doi.org/10.1038/s41560-019-0464-5.
41. Yu, W.; Lin, K.-Y.; Boyle, D. T.; Tang, M. T.; Cui, Y.; Chen, Y.; Yu, Z.; Xu, R.; Lin, Y.; Feng, G.; Huang, Z.; Michalek, L.; Li, W.; Harris, S. J.; Jiang, J.-C.; Abild-Pedersen, F.; Qin, J.; Cui, Y.; Bao, Z. Electrochemical Formation of Bis(Fluorosulfonyl)Imide-Derived Solid-Electrolyte Interphase at Li-Metal Potential. *Nat. Chem.* **2025**, *17* (2), 246–255. https://doi.org/10.1038/s41557-024-01689-5.
42. Betz, J.; Brinkmann, J.; Nölle, R.; Lürenbaum, C.; Kolek, M.; Stan, M. C.; Winter, M.; Placke, T. Cross Talk between Transition Metal Cathode and Li Metal Anode: Unraveling Its Influence on the Deposition/Dissolution Behavior and Morphology of Lithium. *Advanced Energy Materials* **2019**, *9* (21), 1900574. https://doi.org/10.1002/aenm.201900574.
43. Guo, Z.; Cui, Z.; Manthiram, A. Crossover Effects of Transition-Metal Ions on Lithium-Metal Anode in Localized High Concentration Electrolytes. *Adv Funct Materials* **2025**, 2501743. https://doi.org/10.1002/adfm.202501743.
44. Hobold, G. M.; Gallant, B. M. Quantifying Capacity Loss Mechanisms of Li Metal Anodes beyond Inactive Li^0. *ACS Energy Lett.* **2022**, *7* (10), 3458–3466. https://doi.org/10.1021/acsenergylett.2c01845.
45. Yu, Z.; Balsara, N. P.; Borodin, O.; Gewirth, A. A.; Hahn, N. T.; Maginn, E. J.; Persson, K. A.; Srinivasan, V.; Toney, M. F.; Xu, K.; Zavadil, K. R.; Curtiss, L. A.; Cheng, L. Beyond Local Solvation Structure: Nanometric Aggregates in Battery Electrolytes and Their Effect on Electrolyte Properties. *ACS Energy Lett.* **2022**, *7* (1), 461–470. https://doi.org/10.1021/acsenergylett.1c02391.
46. Jang, J.; Wang, C.; Kang, G.; Han, C.; Han, J.; Shin, J.-S.; Ko, S.; Kim, G.; Baek, J.; Kim, H.-T.; Lee, H.; Park, C. B.; Seo, D.-H.; Li, Y.; Kang, J. Miniature Li+ Solvation by Symmetric

Molecular Design for Practical and Safe Li-Metal Batteries. *Nat Energy* **2025**, *10* (4), 502–512. https://doi.org/10.1038/s41560-025-01733-9.

47. Kim, S. C.; Wang, J.; Xu, R.; Zhang, P.; Chen, Y.; Huang, Z.; Yang, Y.; Yu, Z.; Oyakhire, S. T.; Zhang, W.; Greenburg, L. C.; Kim, M. S.; Boyle, D. T.; Sayavong, P.; Ye, Y.; Qin, J.; Bao, Z.; Cui, Y. High-Entropy Electrolytes for Practical Lithium Metal Batteries. *Nat Energy* **2023**, *8* (8), 814–826. https://doi.org/10.1038/s41560-023-01280-1.
48. Ong, M. T.; Verners, O.; Draeger, E. W.; Van Duin, A. C. T.; Lordi, V.; Pask, J. E. Lithium Ion Solvation and Diffusion in Bulk Organic Electrolytes from First-Principles and Classical Reactive Molecular Dynamics. *J. Phys. Chem. B* **2015**, *119* (4), 1535–1545. https://doi.org/10.1021/jp508184f.
49. Kang, Q.; Li, Y.; Zhuang, Z.; Yang, H.; Luo, L.; Xu, J.; Wang, J.; Guan, Q.; Zhu, H.; Zuo, Y.; Wang, D.; Pei, F.; Ma, L.; Zhao, J.; Li, P.; Lin, Y.; Liu, Y.; Shi, K.; Li, H.; Zhu, Y.; Chen, J.; Liu, F.; Wu, G.; Yang, J.; Jiang, P.; Huang, X. Engineering a Dynamic Solvent-Phobic Liquid Electrolyte Interphase for Long-Life Lithium Metal Batteries. *Advanced Materials* **2024**, *36* (18), 2308799. https://doi.org/10.1002/adma.202308799.
50. Jiang, J.; Li, M.; Liu, X.; Yi, J.; Jiang, Y.; Wu, C.; Liu, H.; Zhao, B.; Li, W.; Sun, X.; Zhang, J.; Dou, S. Multifunctional Additives to Realize Dendrite-Free Lithium Deposition in Carbonate Electrolytes toward Low-Temperature Li Metal Batteries. *Advanced Energy Materials* **2024**, *14* (27), 2400365. https://doi.org/10.1002/aenm.202400365.
51. Hobold, G. M.; Kim, K.-H.; Gallant, B. M. Beneficial *vs.* Inhibiting Passivation by the Native Lithium Solid Electrolyte Interphase Revealed by Electrochemical Li^+ Exchange. *Energy Environ. Sci.* **2023**, *16* (5), 2247–2261. https://doi.org/10.1039/D2EE04203G.
52. Huang, Z.; Lai, J.-C.; Liao, S.-L.; Yu, Z.; Chen, Y.; Yu, W.; Gong, H.; Gao, X.; Yang, Y.; Qin, J.; Cui, Y.; Bao, Z. A Salt-Philic, Solvent-Phobic Interfacial Coating Design for Lithium Metal Electrodes. *Nat Energy* **2023**, *8* (6), 577–585. https://doi.org/10.1038/s41560-023-01252-5.